NUMERICAL SIMULATIONS OF THE FLUX TUBE TECTONICS MODEL FOR CORONAL HEATING

C. MELLOR[1], C. L. GERRARD[1], K. GALSGAARD[2], A. W. HOOD[1] and E. R. PRIEST[1]

[1]*School of Mathematics and Statistics, University of St. Andrews, North Haugh, St. Andrews, Fife KY16 9SS, Scotland;* [2]*Niels Bohr Institute for Astronomy, Physics and Geophysics, Astronomical Observatory, Juliane Maries vej 30, 2100 Kbh Ø, Denmark*
(e-mail: alan@mcs.st-and.ac.uk)

Abstract. In this paper we present results from 3D MHD numerical simulations based on the flux tube tectonics method of coronal heating proposed by Priest, Heyvaerts, and Title (2002). They suggested that individual coronal loops connect to the photosphere in many different magnetic flux fragments and that separatrix surfaces exist between the fingers connecting a loop to the photosphere and between individual loops. Simple lateral motions of the flux fragments could then cause currents to concentrate along the separatrices which may then drive reconnection contributing to coronal heating. Here we have taken a simple configuration with four flux patches on the top and bottom of the numerical domain and a small background axial field. Then we move two of the flux patches on the base between the other two using periodic boundary conditions such that when they leave the box they re-enter it at the other end. This simple motion soon causes current sheets to build up along the quasi-separatrix layers and subsequently magnetic diffusion/reconnection occurs.

1. Introduction

The coronal heating problem is one of the major unsolved problems of solar physics. While the photosphere is at a temperature of approximately 6000 K, the temperature in the corona increases to approximately 1×10^6–2×10^6 K. The heating mechanisms which have been suggested to explain this phenomenon can usually be classified as heating due to magnetic waves or heating due to magnetic reconnection. Wave heating mechanisms include resonant absorption, first suggested as a means of heating the solar corona by Ionson (1978), and phase mixing, suggested by Heyvaerts and Priest (1983). Magnetic reconnection heating mechanisms include nanoflares (Parker, 1988), footpoint braiding (Parker, 1979; Galsgaard and Nordlund, 1996), and reconnection at separators (Longcope, 1996; Galsgaard *et al.*, 2000; Parnell and Galsgaard, 2004). It is likely that a combination of heating mechanisms is responsible for heating the corona, with different mechanisms working in, for example, coronal loops and coronal holes.

In this paper we have carried out numerical simulations to investigate a recently proposed magnetic reconnection heating mechanism. In this "flux tube tectonics" model described by Priest, Heyvaerts, and Title (2002), the movement of magnetic
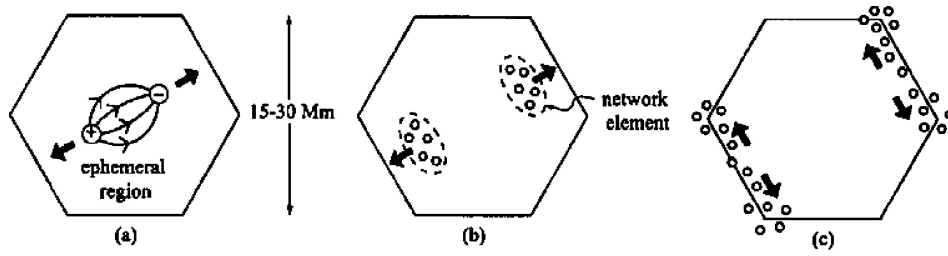
Figure 1. The movement of flux within granules – it rises in the centre, makes its way to the edges of the granules, then along the edges to the vertices. From Priest Heyvaerts, and Title (2002).
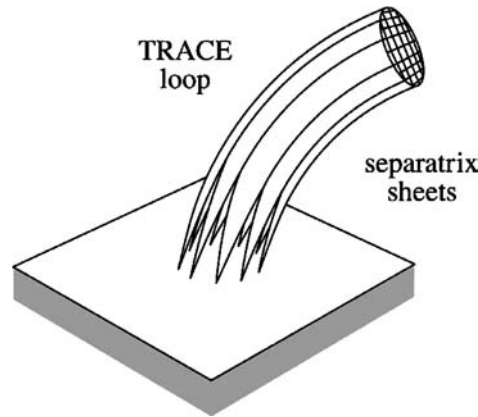

Figure 2. A loop, connecting to the surface in different flux elements. From Priest, Heyvaerts, and Title (2002).

flux fragments in the photosphere drives the formation and dissipation of currents along myriads of separatrix surfaces in the corona.

The photosphere is covered in a "magnetic carpet" of magnetic flux fragments which emerge, fragment, merge and cancel (see e.g. Parnell, 2001, 2002; Simon, Title, and Weiss, 2001). This flux emerges in the centre of granules, makes its way to the edges of the granules and then along the edges to the vertices (see Figure 1). The corona, meanwhile, consists of a multitude of loops of varying sizes. These loops have their footpoints in the photosphere and, therefore, Priest, Heyvaerts, and Title (2002) suggest that each loop connects to the surface in many different flux elements (see Figure 2) and that each flux element will be linked by coronal loops to other flux elements. Separatrix surfaces exist between the fingers connecting a loop to the surface and between loops (see Figure 3). The lateral motions of the magnetic flux fragments in the magnetic carpet will then stress the magnetic field on either side of the separatrix surfaces which is expected to provide strong current concentrations that can then drive reconnection at the separatrix surfaces. Recently it has been shown (Titov *et al.*, 2003; Galsgaard *et al.*, 2003) that in the general
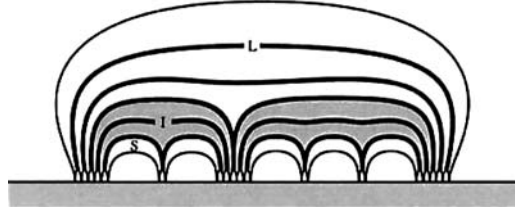
Figure 3. Separatrix surfaces exist between loops and between the fingers connecting a loop to the photosphere. From Priest, Heyvaerts, and Title (2002).

case of hyberbolic flux tubes, defined as the intersection of two quasi-separatrix layers, their presence is not a sufficient condition for fast current growth since the way that the system is stressed determines whether or not the current will grow.

Priest, Heyvaerts, and Title (2002) show, using 2D and 3D models of this scenario, that independent motions of discrete flux elements can generate current concentrations at the separatrix surfaces.

This tectonics model differs from the footpoint braiding since from the start quasi-separatrix layers are present in the magnetic field line topology, while in the braiding experiments these are created by the successive braiding pattern. In addition, the braiding motions are complex whereas the tectonics model considers simple, lateral motions.

In this paper, we will further investigate the proposed tectonics heating mechanism by carrying out 3D magnetohydrodynamic (MHD) simulations based on the "flux tube tectonics" model. In Section 2 we describe the numerical code used, the initial set-up and the boundary driving. In Section 3 we present the results of the numerical runs and compare them with a simple analytical theory and in Section 4 we discuss the results and draw conclusions.

2. Numerical Details, Initial Set-Up and Velocity Profile

The simulations described in this paper were carried out using the 3D MHD code described by Nordlund and Galsgaard (1995). The code solves the non-dimensional MHD equations in the form:

$$\frac{\partial \rho}{\partial t} = -\nabla \cdot \rho \mathbf{u}, \tag{1}$$

$$\frac{\partial \mathbf{B}}{\partial t} = -\nabla \times \mathbf{E}, \tag{2}$$

$$\mathbf{E} = -(\mathbf{u} \times \mathbf{B}) + \eta \mathbf{J}, \tag{3}$$

$$\mathbf{J} = \nabla \times \mathbf{B}, \tag{4}$$

$$\frac{\partial \rho \mathbf{u}}{\partial t} = -\nabla \cdot (\rho \mathbf{u}\mathbf{u} + \underline{\underline{\tau}}) - \nabla P + \mathbf{J} \times \mathbf{B}, \tag{5}$$

$$\frac{\partial e}{\partial t} = -\nabla \cdot (e\mathbf{u}) - P\nabla \cdot \mathbf{u} + Q_{\text{visc}} + Q_{\text{joule}}, \tag{6}$$

where ρ is the density, $\mathbf{u}$ is the velocity, $\mathbf{B}$ is the magnetic field, $\mathbf{E}$ is the electric field, η is the electric resistivity, $\mathbf{J}$ is the electric current, $\underline{\underline{\tau}}$ is the viscous stress tensor, e is the internal energy, $P = (\gamma - 1)e$ is the gas pressure, $T = P/\rho$ is the temperature, Q_{visc} is the viscous dissipation and Q_{joule} is the joule dissipation. We use hyper resistivity and viscosity for most of the experiments described in this paper. The hyper algorithms are described by Nordlund and Galsgaard (1995). The viscosity included in the experiments addresses shock type situations and is of no significant interest to the dynamical evolution. The most important contribution to the resistivity is related to a compression perpendicular to the magnetic field, while there is no common background value of η. Essentially the resistivity is highly localised.

The code is sixth order accurate in space and third order in time. In this paper we use periodic boundary conditions in y and z, to simulate a much larger array of sources, and driven boundary conditions in x (the exact form of the driving will be described below). There are no conditions imposed directly on ρ and e which are updated through the continuity and energy equations respectively. The solenoidal condition is imposed through the use of the staggered grid. The initial value of $\nabla \cdot \mathbf{B}$ is maintained throughout the calculations and we choose the initial field such that $\nabla \cdot \mathbf{B} = 0$.

The initial configuration consists of four equal flux patches and a small background axial field on the top $(x = 1)$ and bottom $(x = 0)$ boundaries of the numerical box. The x-component of the field on the top and bottom boundaries is described by

$$\begin{aligned}
B_x(x = 0, 1) = 0.1 &+ \exp(-350((y - 0.5)^2 + (z - 0.2)^2)) + \\
&+ \exp(-350((y - 0.5)^2 + (z - 0.8)^2)) + \\
&+ \exp(-350((y - 0.2)^2 + (z - 0.5)^2)) + \\
&+ \exp(-350((y - 0.8)^2 + (z - 0.5)^2)). \tag{7}
\end{aligned}$$

We have a small axial background field (given by the 0.1 in Equation (7)) which *removes the presence of real 3D null points in the domain*, and also reduces the steep magnetic gradients near the top and bottom boundaries that would occur if the four sources alone contributed to the flux. As such there are no null points or separatrices, but there are quasi-separatrix layers (QSLs) which separate the regions of different connectivity (Priest and Demoulin, 1995). A potential magnetic field was constructed in the rest of the domain using Equation (7) as the boundary condition. Figure 4 shows B_x on the top and bottom boundaries and Figure 5 shows
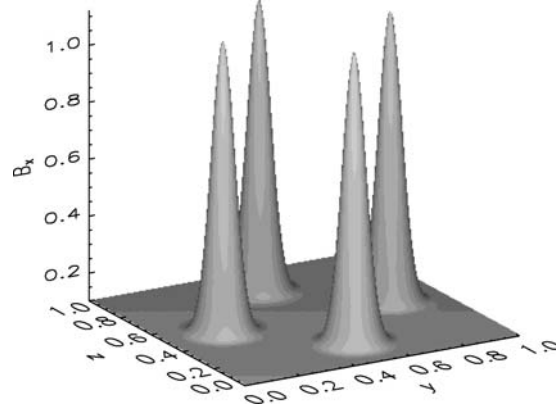
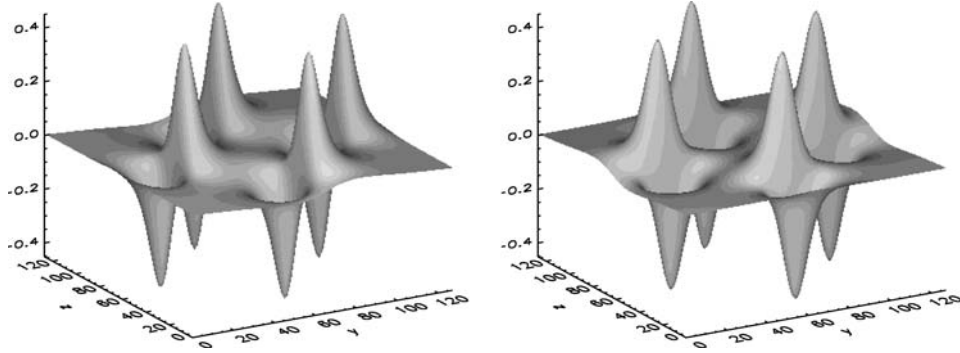*Figure 4.* The initial B_x on the top and bottom boundaries.

Figure 5. The initial B_y (*left-hand side*) and B_z (*right-hand side*) on the top and bottom boundaries.

B_y and B_z on the top and bottom boundaries (note that in this paper the x-direction is the axial direction).

In order to model simple photospheric motions, we drive two of the flux patches on the bottom boundary in a straight line between the other two. The driving speed is -0.03 units which is approximately one fifth of the mean Alfvén speed in the numerical box. The driving profile is taken to be a smooth top-hat function, which advects two of the sources without changing their spatial shape, while not interfering with the two other sources, Figure 6. The photospheric driving function is almost discontinuous. However, the results do not depend on this property. A smooth velocity with a discontinuous photospheric normal field distribution is equivalent to a discontinuous velocity and continuous normal field. This is discussed in more detail in Section 3.2. The other two velocity components (v_x and v_z) are taken to be zero on the base. All velocity components are zero on the upper boundary.
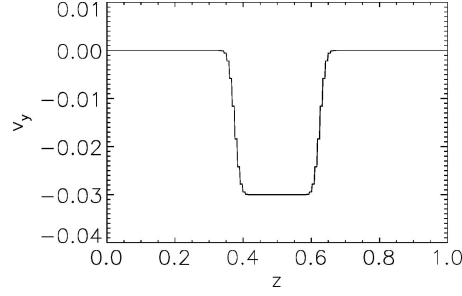
Figure 6. The driving velocity on the bottom boundary.

3. Results

The experiment was run for grid resolutions of 64^3, 128^3 and 256^3. We define $t_A = 1$ as the time to travel a distance of 1 (the box length) at a speed of 1 (the average Alfvén speed in the box is approximately 0.15 initially and an Alfvén speed of 1 would occur near the peak of any of the flux patches). Each resolution was run for 15.7 Alfvén times (t_A), meaning that the flux patches were driven a total distance of 0.47, the periodic boundary conditions ensuring that when a footpoint left one side of the box, another entered through the opposite side. During this time, the Alfvén waves travelling along the field lines had gone from the bottom of the box to the top, and reflected back to the bottom, and were approximately halfway up to the top again, allowing free and rapid propagation of information in the box. A further simulation was run on a 128^3 grid, but with the driving speed of -0.01. This allows us to compare what happens when the number of travel times is increased, allowing information to propagate further for the same footpoint displacement.

3.1. CURRENT SHEET FORMATION

During the simulation, two sheets of current are seen to build up in the centre of the numerical box. These correspond to rapid changes in B_y in the x direction. The sheets of current were checked for scaling to see whether they represented a current sheet (theoretically an infinitesimally thin region of infinite current, which is significant because even the small coronal values of resistivity will trigger reconnection under this condition) or a current concentration which saturates at a finite value and only triggers reconnection for a finite value of the resistivity. If they are current sheets, the maximum value of the current will scale linearly with resolution, and so will double with each higher grid size in this experiment. Table I shows the maximum values of $|j|$ within the sheets of current throughout the simulation and compares them with the values we expect if we scale the observed 64^3 value with the grid resolution.

Table I implies that the maximum currents do scale with grid resolution, which points in favour of current sheet formation. As will be shown later, the steepness of

TABLE I

Comparing the scaling of $|j_{max}|$ for the different grid resolutions.

Grid resolution	Expected value of $|j_{max}|$	Observed value of $|j_{max}|$
64^3	2.919	2.919
128^3	5.838	4.996
256^3	11.676	10.970

the driving profile will have implications for the growth of the current for a given shear distance. The top-hat driving profile is designed such that the width remains constant in space, implying that higher numerical resolution gives a better resolved profile. It may then be expected that for even higher resolutions runs than we have been able to do, the current magnitude may saturate. The numerical diffusion algorithms allow structures to collapse to a minimum grid resolution and will for increasing resolution allow a current sheet to collapse to the same grid resolution – hence the $1/\mathrm{d}x$ growth of the current.

We compare the current sheets formed for these runs with those formed for the 128^3 run where the footpoints were driven at one third of the speed of the previous runs. This allows information to propagate up and down the numerical box three times as often before the footpoints are driven to the same locations, thus allowing the magnetic field more opportunity to relax.

Figure 7 shows a plot of $|j_{max}|$ in the plane $x = 0.5$ for the 128^3 runs with a driving speed of -0.03 (solid line) and -0.01 (dashed line). The current jumps in value initially as the information propagates through this middle plane. As the footpoint displacement increases, the middle plane is being affected from above and below, so the current grows more smoothly. This can be explained in terms of a simple damped Alfvén wave. We carry out a simple analytical investigation of this. Assume the footpoint motion, v_y generates a perturbed magnetic field component B_y. The maximum current will be related to the "discontinuities" in B in the x direction and, therefore, will behave similarly to B_y in time. Solving the linearised
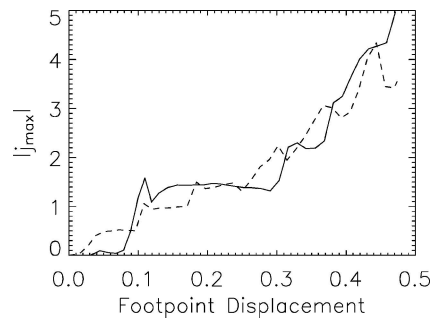

Figure 7. A plot of j_{max} in the plane $x = 0.5$ for the 128^3 runs with a driven speed of -0.03 (solid line) and -0.01 (dashed line).

momentum and induction equations,

$$\frac{\partial v_y}{\partial t} = \frac{\partial B_y}{\partial x} \tag{8}$$

and

$$\frac{\partial B_y}{\partial t} = \frac{\partial v_y}{\partial x} + \eta \frac{\partial^2 B_y}{\partial x^2}, \tag{9}$$

subject to $v_y(0, t) = -1$, $v_y(1, t) = 0$, $v_y(x, 0) = 0$, $\frac{\partial v_y}{\partial t}(x, 0) = 0$, $B_y(x, 0) = 0$ and $\frac{\partial B_y}{\partial x}(0, t) = 0$ gives

$$v_y = -1 + x + \sum_1^\infty \sin(n\pi x) e^{-\eta n^2 \pi^2 t/2} \times$$
$$\times \left(\frac{2}{n\pi} \cos(n\pi \sqrt{1 - n^2 \pi^2 \eta^2} t) + \frac{\eta}{\sqrt{1 - n^2 \pi^2 \eta^2}} \sin(n\pi \sqrt{1 - n^2 \pi^2 \eta^2} t) \right), \tag{10}$$

and B_y can be calculated from (8). Figure 8 shows a plot of B_y against time for $x = 0.5$ and $\eta = 0.01$ and demonstrates that B_y has the same behaviour as the
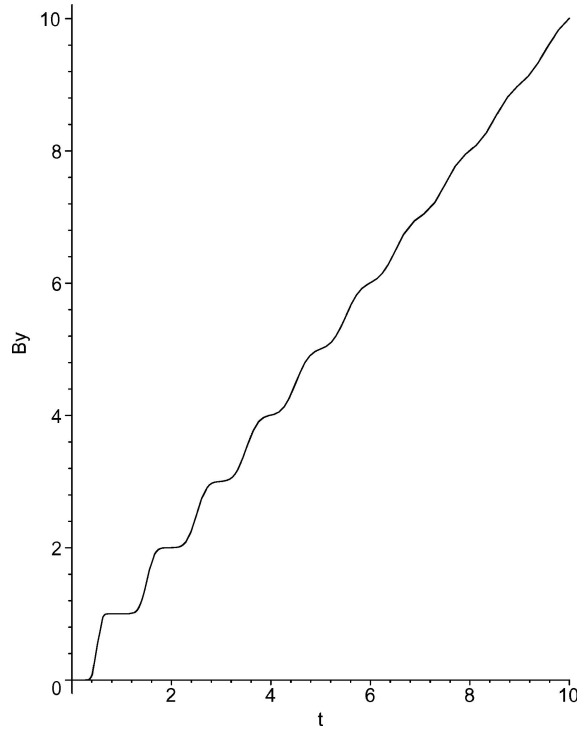

Figure 8. A plot of B_y in the plane $x = 0.5$ against time assuming a damped Alfvén wave propagation showing good agreement with Figure 7.
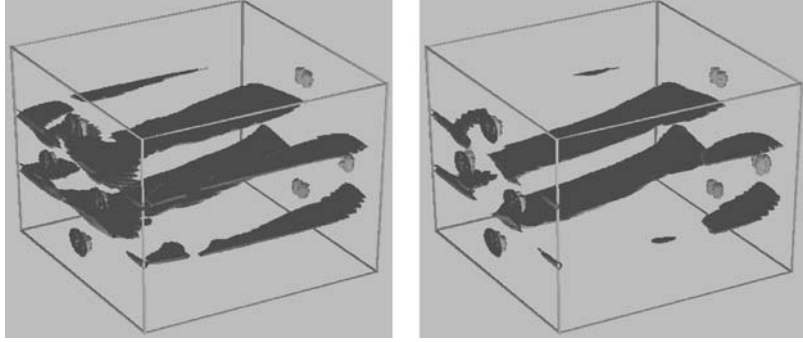
Figure 9. Plots of the current isosurface $|\mathbf{j}| = 2$ for the two different driving speeds at a footpoint displacement of 0.47. The quicker speed -0.03 is shown *on the left* and the slower speed -0.01 *on the right*. Both runs have 128^3 gridpoints.

current in Figure 7. It starts as a series of steps corresponding to propagating Alfvén waves reflecting off the boundaries. Diffusion smoothes out these steps in time leaving a linear increase in B_y with respect to time. Thus, the footpoint velocity results in a linear increase in B_y and we can assume that the field is evolving through a sequence of equilibria.

Figure 9 shows isosurfaces of $|\mathbf{j}| = 2$ for the same two driving speeds and a footpoint displacement of 0.47, the quicker driving speed being on the left. In the case of the faster driving, there is slightly more current build-up near the boundaries, but the two main sheets of current are the same.

The current in both cases is growing at approximately the same rate for a given displacement and the isosurfaces of current look very similar so it would appear that for footpoint displacements up to the values we have investigated here, the speed at which the footpoints are driven does not affect the evolution of the field.

The 129^3 simulation with driving speed of -0.03 was run longer, up to a time of $43.02t_A$ (equivalent to a footpoint displacement of 1.29). Figure 10 shows contours of $|\mathbf{j}| = 3.6$ in the middle ($x = 0.5$) plane at $t = 37.2t_A$. This is half of the maximum current in the plane and gives a good idea as to how thick the sheets of current are.
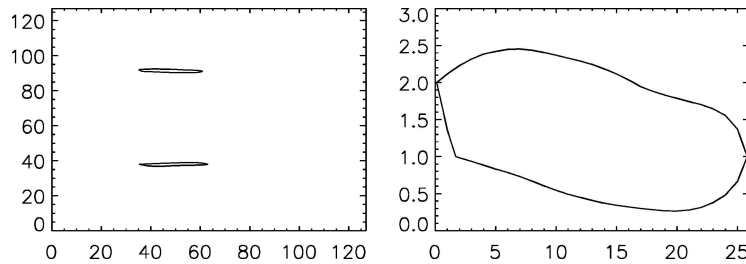

Figure 10. Contours of $|\mathbf{j}| = 3.6$ showing that the current sheet is thin. *Left*: the whole of the $x = 0.5$ plane. *Right*: a close-up of the upper contour, showing it to be fewer than three grid points wide (128^3 experiment).
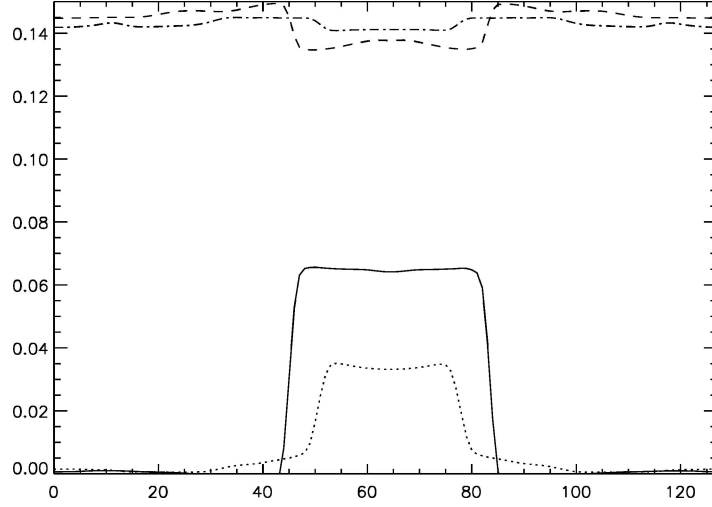
Figure 11. A plot of B_y and B_x against z (in gridpoints) at $t = 5.08$ and $t = 14.32t_A$ in the plane $x = 0.5$, $y = 0.5$. The *unbroken line* is B_y at $t = 14.32$, the *dashed line* is B_x at the same time, the *dotted line* is B_y at $t = 5.08$ and the *dot-dashed line* is B_x at $t = 5.08$ (128^3 experiment).

The second plot is a close-up of the top contour in the first plot, showing the sheet to be fewer than three grid points thick. A thin, localised current is indicative of current sheet formation.

Figure 11 shows B_y and B_x plotted against z in the plane $x = 0.5$, $y = 0.5$. The current layer can clearly be seen by the jumps in B_y and B_x as would be expected. Both components are plotted at two times, $t = 5.08$ and $t = 14.32t_A$. At $t = 5.08t_A$ the current layers are at $z = 0.61$ and $z = 0.39$ but by $t = 14.32t_A$ they have moved outwards to $z = 0.66$ and $z = 0.34$. This figure illustrates that the components of the magnetic field behave as would be expected in a current sheet, jumping in value through the current layer. The rapid change in B_y and B_z is a result of the imposed photospheric flux distribution and the shearing velocity profile. Figure 12 shows j_x and j_y at $t = 14.32t_A$. The peaks in j_x and j_y correspond to the jumps in B_x and B_y. Integrating j_x from $z = 0.5$ to 1.0 gives the total positive current in the x direction as 0.072. This is in good agreement with the jump in B_y of 0.070 given by the simulations. Similarly integrating j_y gives 0.012 which is in good agreement with the jump in B_x of 0.014. Figure 11 also indicates that the current layers are moving away from the centre of the driving profile as the simulation continues. Notice that the jump in B_y is negative and corresponds to a positive value of j_x. The jump in B_x is positive as is the sign of j_y. Figure 13 shows the position of one of the current layers against time and the outward movement can now clearly be seen. If this current layer is at z^*, the other is at $(1 - z^*)$. In the next subsection we will show that this outwards drift of the current concentrations can be predicted using a simple analytical model.
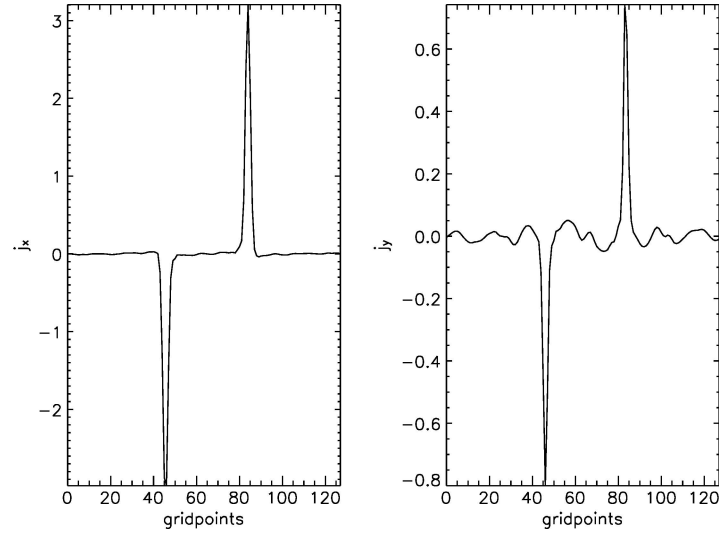
Figure 12. A plot of j_x (*left-hand side*) and j_y (*right-hand side*) against z (in gridpoints) at $t = 14.32t_A$ showing the peaks which correspond to the jumps in B_y and B_x respectively (128^3 experiment).
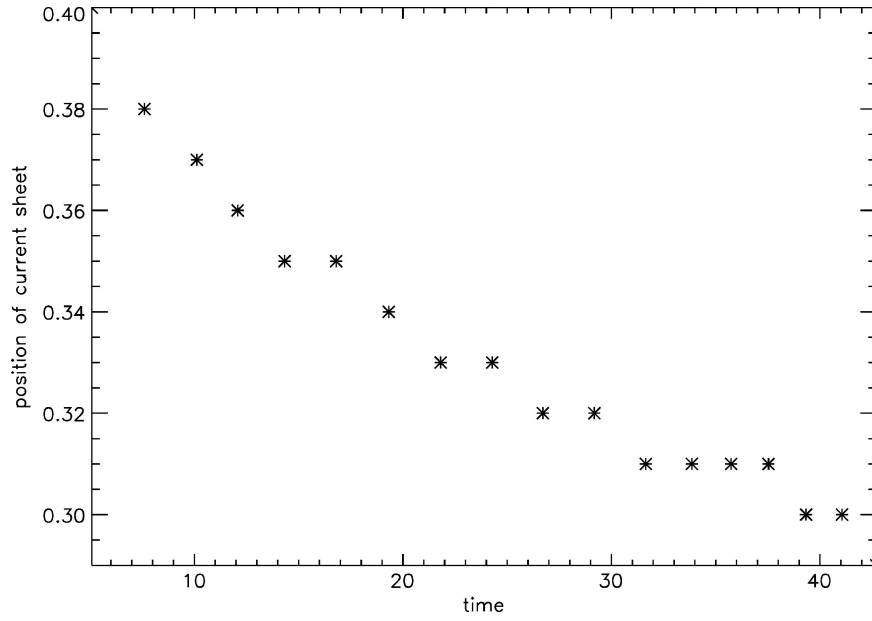

Figure 13. A plot of the position, in gridpoints, of one of the current layers against time showing the outward drift of the current layer over the course of the simulation (128^3 experiment).

3.2. 1D ANALYTICAL MODEL

We can model the current sheet formation using a 1D analytical model. We assume a flux function of the form

$$\mathbf{A} = (0, A(x, z), 0) \tag{11}$$

and, with the shearing motions introducing a y-component, the magnetic field can be expressed as

$$\mathbf{B} = \left(-\frac{\partial A}{\partial z}, B_y(A), \frac{\partial A}{\partial x} \right). \tag{12}$$

Now, the footpoint displacement is given by

$$v_y(A)t = \delta(A) = \int_{x=0}^{x=H} \frac{B_y(A)}{B_x} \Big|_{A=\text{const}} dx, \tag{13}$$

and since $B_y(A)$ is independent of x this can be written as

$$\delta(A) = B_y(A) \int_{x=0}^{x=H} -\frac{1}{\left(\frac{\partial A}{\partial z} \right)} \Big|_{A=\text{const}} dx. \tag{14}$$

To approximate the integral in (14), we make the following assumption. The magnetic field rapidly expands from a single flux concentration until it meets the field from the neighbouring flux sources. The expansion ceases at a height that is related to the separation distance on the photosphere. Then the field becomes uniform in the x direction until it approaches the other footpoint, where the reverse process occurs. The uniform region means that the flux function can be replaced by a function of z alone. Thus, $A = A(z)$, $B_x = -\partial A/\partial z$ and $B_z = 0$. Notice that B_x is now independent of x (and is actually a function of A) and so the integral can be approximated by $-H/(\partial A/\partial z)$. Thus, the footpoint displacement can be expressed as a function of A. This is similar to the approach used by Lothian and Hood (1989) and Browning and Hood (1989) for the cylindrical case. Thus, the footpoint displacement can be expressed as

$$\delta(A) = -\frac{H B_y(A)}{dA/dz}. \tag{15}$$

So the footpoint displacement is a fixed property of the field lines and is a known function of the flux function, A. All that is necessary is to take the imposed footpoint displacement, which is a function of z at the photosphere, and the flux function, which is also a function of z, and express δ as a function of A. Then,

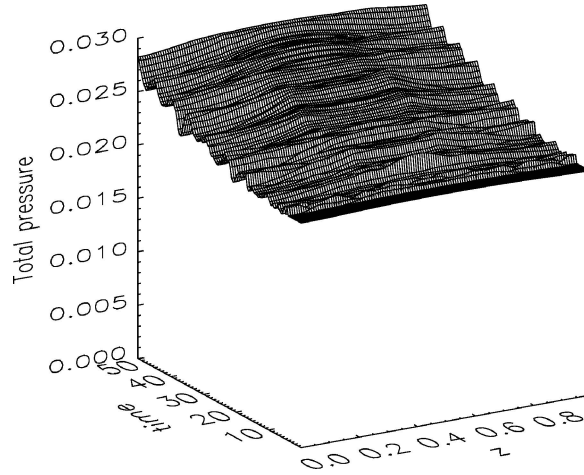$$B_y(A) = -\frac{\delta(A)}{H} \frac{dA}{dz}. \tag{16}$$

Figure 14. A plot of $P + B^2/2$ as a function of z (in the direction across the current sheet) and time for the simulation. This shows that the total pressure increases with time, while a near pressure balance is maintained in the z direction for all times, just as predicted by the theory.

Since the field is straight, there is no magnetic tension and the equilibrium reduces to constant magnetic pressure. Hence,

$$\left(\frac{\mathrm{d}A}{\mathrm{d}z}\right)^2 + B_y^2(A) = \text{constant}. \tag{17}$$

Figure 14 shows a surface plot of $P + B^2/2$ against z and time demonstrating that the total pressure is indeed constant across the numerical domain. Since the plasma β is small we can neglect the gas pressure and take B^2 constant (equal to k^2). The constant does increase with time as indicated in Figure 14.

Using the footpoint displacement calculated in (16) then (17) can be written as

$$\left(\frac{\mathrm{d}A}{\mathrm{d}z}\right)^2 \left[1 + \left(\frac{\delta(A)}{H}\right)^2\right] = k^2. \tag{18}$$

(18) is solved subject to the boundary conditions, consistent with the numerical simulations,

$$A(L/2) = 0, \tag{19}$$
$$A(L) = B_{x0}L/2. \tag{20}$$

Note that the total flux is $A(L) - A(0) = B_{x0}L$.

Figure 15 shows the footpoint displacement as a function of A. Since this is the form of a step function we need to consider two regions of the domain, $A \leq B_{x0}a/2$ and $A > B_{x0}a/2$.
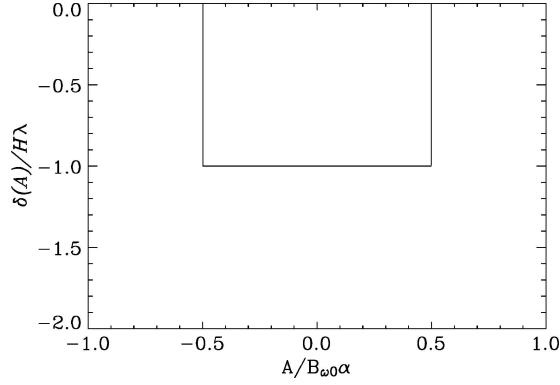
Figure 15. The photospheric footpoint displacement as a function of *A*.

For $A \le B_{x0}a/2$ we have

$$\left(\frac{dA}{dz}\right)^2 [1 + \lambda^2] = k^2, \tag{21}$$

where $\delta/H = v_y t/H = \lambda$. Thus,

$$A = \frac{k}{\sqrt{1 + \lambda^2}}(z - L/2). \tag{22}$$

For $A > B_{x0}a$,

$$\left(\frac{dA}{dz}\right)^2 = k^2, \tag{23}$$

which gives

$$A = k(z - L/2) + M, \tag{24}$$

and since $A(z = L) = B_{x0}L/2$ (the total flux) we have, $M = B_{x0}L/2 - kL/2$.

Finally, continuity of *A* at the interface, i.e., at $A = B_{x0}a/2$ where

$$z = L/2 + \frac{B_{x0}a\sqrt{1 + \lambda^2}}{2k}, \tag{25}$$

gives

$$M = B_{x0}a(1 - \sqrt{1 + \lambda^2})/2 \tag{26}$$

and

$$k = B_{x0} + B_{x0}\frac{a}{L}(\sqrt{1 + \lambda^2} - 1). \tag{27}$$

Hence, the total magnetic pressure is $k^2/2$ and so,

$$\frac{B^2}{2} = \frac{B_{x0}^2}{2}\left(1 + \frac{a}{L}(\sqrt{1 + \lambda^2} - 1)\right)^2. \tag{28}$$

Finally this gives us

$$A = \frac{B_{x0}\left(1 + \frac{a}{L}(\sqrt{1 + \lambda^2}) - 1\right)(z - L/2)}{\sqrt{1 + \lambda^2}}, \quad A \leq B_{x0}a/2, \tag{29}$$

$$A = B_{x0}\left(1 + \frac{a}{L}(\sqrt{1 + \lambda^2} - 1)\right)(z - L/2) + B_{x0}\frac{a}{2}\left(1 - \sqrt{1 + \lambda^2}\right),$$
$$A > B_{x0}a/2. \tag{30}$$

We can now use this expression for the flux function to make predictions about the simulation results.

We can predict that the current sheets are likely to occur in the region where $A = B_{x0}a/2$, i.e., at

$$z = \frac{L/2 \pm a\sqrt{1 + \lambda^2}}{2\left(1 + \frac{a}{L}(\sqrt{1 + \lambda^2} - 1)\right)}, \tag{31}$$

and will, therefore, move outwards as the shear increases in agreement with the simulations. This shows that this simplified analytical model can reproduce some of the physical behaviour demonstrated in the numerical simulation.

Furthermore, we can use the 1D model to predict how the magnetic field strength should vary with time. The total field strength is given by k, and so by substituting $a = 0.125$, $L = 1$, $H = 1$, $\lambda = Hv_{y0}t = 0.03t$ into k we can obtain an expression for the field strength. In Figure 16 we have plotted the mean of B^2 from the numerical simulation at $x = 0$, $y = 0$ against time and have over-plotted k^2. It can be seen that the two show good agreement. Thus, the 1D model gives a good prediction of the behaviour of the magnetic field in time.

In the discussion above we assumed a uniform field and discontinuous velocity which makes the velocity a discontinuous function of A (this is equivalent to taking a discontinuous flux distribution and applying a continuous velocity which is how the flux tube tectonics model is usually expressed). We have seen that this analytical model is in good agreement with the numerical results. However, due to numerical constraints we had to add a background axial field to the numerical simulations, so we now consider the effect of a weak uniform background field to the initial discrete flux sources. This gives a continuous flux distribution and removes the photospheric null point. Consider a simple analytical model with the photospheric velocity and flux function profiles given by

$$v_y(0, 0, z) = v_y(\tilde{z}), \quad A(0, 0, z) = A(\tilde{z}),$$

where $\tilde{z}$ stands for the distance in the z-direction *at the photospheric surface*. Rearranging, these allows us to write
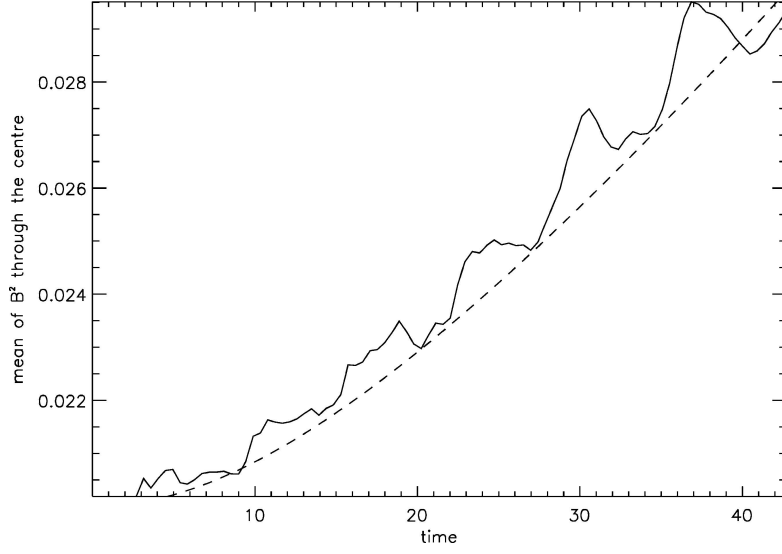
$$v_y = v_y(A).$$

Figure 16. A plot of the mean of B^2 (*solid curve*) at $x = 0$, $y = 0$, for a driving velocity of -0.03, against time with the analytical B^2 from (27) (*dashed curve*) demonstrating the good agreement between theory and numerics, note that a time $t = 40$ is equivalent to a displacement of 1.2.

As above, this velocity allows us to calculate the footpoint displacement and the functional form of $B_y(A)$. Thus, the flux function, in the region where the field has expanded and become independent in x, can be expressed as a function of z as

$$\frac{dA}{dz} = \frac{k}{\sqrt{1 + (\delta(A)/H)^2}}. \tag{32}$$

Note that z is used to describe the distance at the coronal level and $\tilde{z}$ the distance at the photospheric surface. The flux function can be formally obtained by integrating to give

$$k\left(z - \frac{L}{2}\right) = \int_0^A \sqrt{1 + (\delta(A_1)/H)^2}\,dA_1$$

$$= \int_{L/2}^{\tilde{z}_1} \sqrt{1 + (\delta(\tilde{z})/H)^2}\frac{dA_1}{d\tilde{z}}\,d\tilde{z},$$

where $A = A(\tilde{z}_1)$. To calculate the current in the corona, differentiate (32) with respect to z to obtain

$$\frac{d^2A}{dz^2} = -\frac{k\delta(A)}{(1 + (\delta(A)/H)^2)^{3/2}H^2} \times \frac{d\delta}{dA} \times \frac{dA}{dz}.$$

We use (32) to express dA/dz in terms of A. Now since δ is known as a function of $\tilde{z}$, it is possible to rewrite

$$\frac{d\delta}{dA} = \frac{d\delta/d\tilde{z}}{dA/d\tilde{z}},$$

so that the coronal current is expressible as

$$\frac{d^2A}{dz^2} = -\frac{k^2\delta(A)}{(1 + (\delta(A)/H)^2)^2 H^2} \times \frac{d\delta}{d\tilde{z}} \times \frac{1}{dA/d\tilde{z}}. \tag{33}$$

There are two possibilities for forming a current sheet in the corona, given by the two terms $d\delta/d\tilde{z}$ and $dA/d\tilde{z}$. Thus, either $d\delta/d\tilde{z}$ is infinite, corresponding to a discontinuous photospheric velocity profile, or $dA/d\tilde{z} = 0$, in which case the photospheric magnetic field distribution is discontinuous. When neither of these conditions is satisfied, the coronal current will reach a maximum value but will not initially form a current sheet.

The value of the maximum coronal current depends on the flux and velocity profiles chosen. As a simple illustration, consider

$$A(\tilde{z}) = B_0\tilde{z} + \frac{\sqrt{\pi}}{2}(\text{erf}(\alpha(\tilde{z} - 0.5)) + \text{erf}(\alpha(\tilde{z} - 0.2)) + \text{erf}(\alpha(\tilde{z} - 0.8))),$$

and

$$\delta(\tilde{z}) = \lambda(\tanh(d(\tilde{z} - 0.375)) - \tanh(d(\tilde{z} - 0.625))). \tag{34}$$

α and d can be chosen to adjust the sharpness of both the flux and velocity profiles. To compare with the results of our numerical simulation, we take $\alpha^2 = 350$ and $d = 100$. B_0 is the strength of the uniform background field. Using the above analysis, the maximum current is shown in Figure 17. Note that the maximum current tends to infinity as B_0 tends to zero.
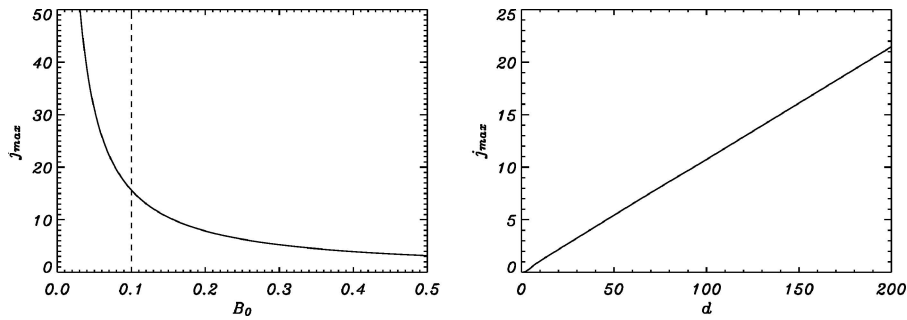

Figure 17. The maximum current from (33) is shown as a function of B_0, the background magnetic field strength with $d = 100$ in (34) (*left-hand side*) and the maximum current is plotted against d for $B_0 = 0.1$ (*right-hand side*).

3.3. RECONNECTION OR DIFFUSION?

As shown in Section 3.1 there is evidence in the numerical results of current sheet formation along the QSLs. This suggests that with resistivity included in the experiments some kind of energy release process, e.g., reconnection or diffusion, may occur. We investigate this using two further experiments. The 256^3 simulation is continued up to $t = 50t_A$ (this is equivalent to a footpoint displacement of 1.5) using the hyper-resistivity described in Nordlund and Galsgaard (1995). Also a second experiment is carried out using a constant resistivity, $\eta = 0.0005$, again on a 256^3 grid. This allows us to investigate the effect of the form of the resistivity on the results.

The first difference between the hyper-resistivity experiment and constant resistivity experiment is that in the former the width of the current concentration is much smaller – close to the grid resolution – than in the latter which contains many grid points. In addition, the current grows more slowly and saturates at a much lower value for the constant resistivity experiment as shown in Figure 18. In both cases the magnetic field lines, in the central region of the advection flow, are advected ideally with the imposed driving flow. In the hyper-resistivity case this behaviour is followed almost out to the transition region between the two flow regions. This happens because the current concentration is kept to a minimum grid point resolution all the time – allowing the current to grow nearly linearly with time as indicated by the dashed line in Figure 18. In contrast to this, the constant resistivity case differs in that it distributes the current over an increasing number of grid points with time allowing only a near constant current value after a given shear distance to buildup. Given enough time this process would saturate and a steady state due to a balance between Joule dissipation and Poynting flux would be reached.

There is no sign of significant dynamic behaviour linked to fast magnetic reconnection in the constant resistivity experiment, i.e., there is no indication of super-Alfvénic flows, rapid changes in field line connectivity or fast energy
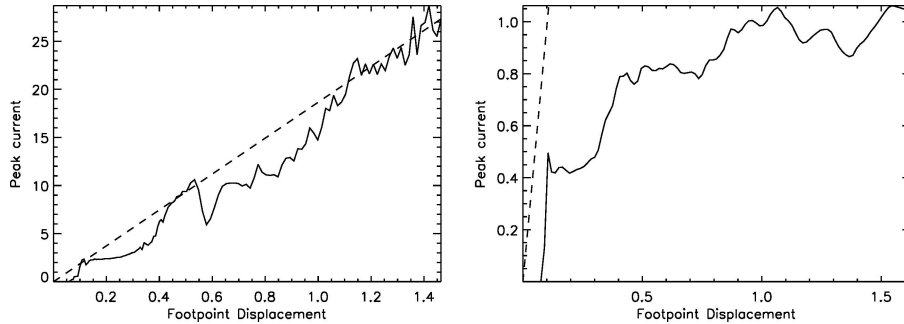

Figure 18. Left: plot of maximum current against time for the hyper-resistivity experiment. *Right*: plot of maximum current against time for the constant resistivity experiment. These show that the current grows more slowly and saturates at a much lower value for the constant resistivity experiment.

release. There is simple dissipation and smoothing of the current throughout the experiment.

Initially in the hyper-resistivity experiment there is no sign of reconnection taking place. For most of the experiment, the magnetic structures around the current sheets evolve smoothly without any sign of rapid disruptions capable of producing fast flow velocities. This changes at the very end of the experiment when there are signs of fast dynamic evolution with indications of changes in field line mapping and of disruption of the current sheets. This more "explosive" behaviour suggests that fast reconnection does occur at the end of the hyper-resistivity experiment. It also raises the question of what triggered the reconnection in the hyper-resistivity experiment. One possibility is the non-linear development of the tearing mode instability. A simple estimate suggests that the tearing mode may be triggered if $L/a > 2\pi$ where L is the loop length and a the thickness of the current concentration. Assuming that the loop has a length given by the length of the box, 1.0, and since the current concentration is a few gridpoints across (say $6-8$) we would obtain a ratio of $L/a = 32-42$ which is clearly above the threshold of 2π. However, this may be an overestimate. Therefore, a second estimate assumes that the effective length of the sheet is between 1/3 and 1/4 of the domain size. This gives a value of 8–10 that is close to the limit of 2π. These rough calculations suggest that the tearing mode is a possible candidate for triggering reconnection for the hyper-resistivity experiment. Since the current concentration is much wider in the constant resistivity experiment, it suggests that $L/a < 2\pi$ and, therefore, the tearing mode would not be triggered for that form of resistivity within the experimental run-time.

These results suggest that, in the case of constant resistivity at the present spatial resolution and for the present run-time, there is only diffusion contributing to the heating of the plasma. Only in the case where the constant resistivity is significantly decreased, can the current buildup be fast enough to trigger a tearing mode, with an associated fast dynamical evolution phase. For the hyper-resistivity case both reconnection and diffusion occur although the reconnection only occurs at the end of the experiment where the structure of the current sheet has reached a state that initiates a tearing mode instability. This suggests that the nature of the heating is dependent on the form of the resistivity (Roussev, Galsgaard, and Judge, 2002) but in both cases some of the free magnetic energy, injected through the boundary Poynting flux, is released in the coronal part of the loop. This is verified by looking at the difference in the growth of the magnetic energy and the related Joule dissipation for the two experiments. It is found that the constant resistivity case releases more magnetic energy through magnetic dissipation than the hyper-resistive case. The form and amplitude of the magnetic diffusion will therefore be of significant importance for both the plasma heating and the structure of the local magnetic field in which the diffusion takes place.

4. Conclusions

In this paper we have presented results for simple 3D numerical simulations based on the recently proposed flux tube tectonics model for coronal heating. Priest, Heyvaerts, and Title (2002) suggested that simple lateral motions of magnetic flux fragments in the photosphere drive the formation and dissipation of currents along the separatrix surfaces in the corona. Each coronal loop will connect to the photosphere in different flux elements and separatrix surfaces will form between the fingers connecting a loop to the surface and between individual loops. Simple motions of the flux fragments will then drive the formation of current sheets at these separatrix surfaces and will drive reconnection.

We have used a 3D MHD code (Nordlund and Galsgaard, 1995) which is 6th order accurate in space and 3rd order accurate in time to investigate this heating mechanism. We have placed 4 equal flux patches on the top and bottom of the numerical domain and constructed the *potential* field connecting them. In addition we have included a small background axial field throughout the domain. Due to this background field there are no separatrices but instead there are quasi-separatrix layers which separate the regions of connectivity. We drive two of the flux patches on the base between the other two and since we are using periodic boundary conditions when they pass out of one end of the numerical box they enter at the other allowing us to simulate a much larger array of sources. We run the code on three different resolutions up to $t = 15.7t_A$ and one run with slower driving velocity for comparison. Finally two high resolution runs are made to investigate the dependence of the results on the from of magnetic resistivity. We also compare the numerical results to some analytical predictions.

We find that concentrations of current build up as the configuration evolves. If we test the scaling of the current with grid resolution for the hyper-resistivity setup we find that it scales almost linearly which suggests current sheet formation. Driving at a slower speed has no significant effect on the current sheet formation. We find that the current is very thin and localised which is another indication of current sheet formation. Finally B_x and B_y can be seen to jump in value through the current sheet as would be expected. A close investigation of the current sheets reveals that they move outwards as the simulation progresses. This can, in fact, be predicted using a 1.5D model, as can that fact that the configuration remains in near pressure balance.

Since we obtain current sheets and we include resistivity we would expect some type of magnetic energy release to take place and we do find indications that it does so. To investigate this we carry out two experiments, one with hyper resistivity and one with constant resistivity. We find evidence of reconnection at the end of the hyper-resistivity experiment: dynamic evolution, disruption of the current sheet, significant changes in field line connectivity. However, there is no indication of such "explosive" energy release for the constant resistivity experiment. This suggests that the form of the resistivity affects the nature of the

energy release (Roussev, Galsgaard and Judge, 2002): diffusion and reconnection occur for the hyper-resistivity experiment, diffusion alone releases the energy in the constant resistivity experiment. One possible trigger for the reconnection in the hyper-resistivity experiment is the tearing mode instability.

However, whether the energy is released due to reconnection or diffusion it will heat the plasma. How much heating is produced in this scenario and how it compares with observations will be investigated in detail in the future.

To summarise the conclusions:

- It appears that simple lateral motions applied to a non-uniform magnetic field configuration can lead to a build-up of current.
- The current concentrations have features which are indicative of current sheet formation.
- The location of the current concentrations moves outwards in the course of the simulation as predicted by 1.5D analytical theory to maintain a pressure balance in the system.
- In the hyper-resistivity experiment both diffusion and reconnection (possibly triggered by the tearing mode instability) occur. For the constant resistivity experiment only diffusion occurs. This suggests that the flux tube tectonics model can lead to heating of the plasma, but that the form of the heating may depend on the structure of the resistivity (Roussev, Galsgaard and Judge, 2002).
- It seems, from these simple numerical simulations, that some amount of heating can be produced by this model.

Acknowledgements

References

Browning, P. K. and Hood, A.W.: 1989, *Solar Phys.* **124**, 271.
Galsgaard, K. and Nordlund, A.: 1996, *J. Geophys. Res.* **101**, 13445.
Galsgaard, K. *et al.*: 2000, *Astron. Astrophys.* **362**, 383.
Galsgaard, K. *et al.*: 2003, *Astrophys. J.* **595**, 506.
Heyvaerts, J. F. and Priest, E. R.: 1983, *Astron. Astrophys.* **117**, 220.
Ionson, J. A.: 1978, *Astrophys. J.* **226**, 650.

Longcope, D. W.: 1996, *Solar Phys.* **169**, 91.

Lothian, R. M. and Hood, A. W.: 1989, *Solar Phys.* **122**, 227.

Nordlund, A. and Galsgaard, K.: 1995, *A 3D MHD code for Parallel Computers*, Technical Report, Astronomical Observatory, Copenhagen University.

Parker, E. N.: 1979, *Cosmical Magnetic Fields*, Oxford University Press, Oxford.

Parker, E. N.: 1988, *Astrophys. J.* **330**, 474.

Parnell, C. E.: 2001, *Solar Phys.* **200**, 23.

Parnell, C. E.: 2002, *Monthly Notices Royal Astron. Soc.* **335**, 389–398.

Parnell, C. and Galsgaard, K.: 2004, *Astron. Astrophys.* **428**, 595.

Priest, E. R. and Demoulin, P.: 1995, *J. Geophys. Res.* **100**, 23443–23464.

Priest, E. R., Heyvaerts, J. F. and Title, A. M.: 2002, *Astrophys. J.* **576**, 533.

Roussev, I., Galsgaard, K. and Judge, P. G.: 2002, *Astron. Astrophys.* **382**, 639–649.

Simon, G. I., Title, A. M. and Weiss, N. O.: 2001, *Astrophys. J.* **561**, 427.

Titov, V. S. *et al.*: 2003, *Astrophys. J.* **582**, 1172.